Electronic Supplementary Material (ESI) for Journal of Materials Chemistry A.

Supporting Information

A multifunctional cathode sodiation additive for high-performance sodium ion batteries

Rui Zhang[a, b], Yan Wang[a], Runnan Liu[a], Dan Sun[a]*, Yougen Tang[a], Zhiyong Xie[b]*, Haiyan Wang[a]*

[a] *Hunan Provincial Key Laboratory of Chemical Power Sources, Hunan Provincial Key Laboratory of Efficient and Clean Utilization of Manganese Resources, College of Chemistry and Chemical Engineering, Central South University, Changsha, 410083, P.R. China*

[b] *Powder Metallurgy Institute, Central South University, Changsha, 410083, P.R. China*

*Corresponding Authors:

*E-mail: sundan4330@csu.edu.cn (Dan Sun)

*E-mail: xzy507@csu.edu.cn (Zhiyong Xie)

*E-mail: wanghy419@csu.edu.cn (Haiyan Wang)

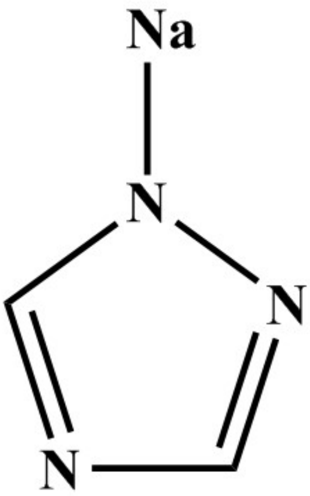

Fig. S1. The chemical formula of TS

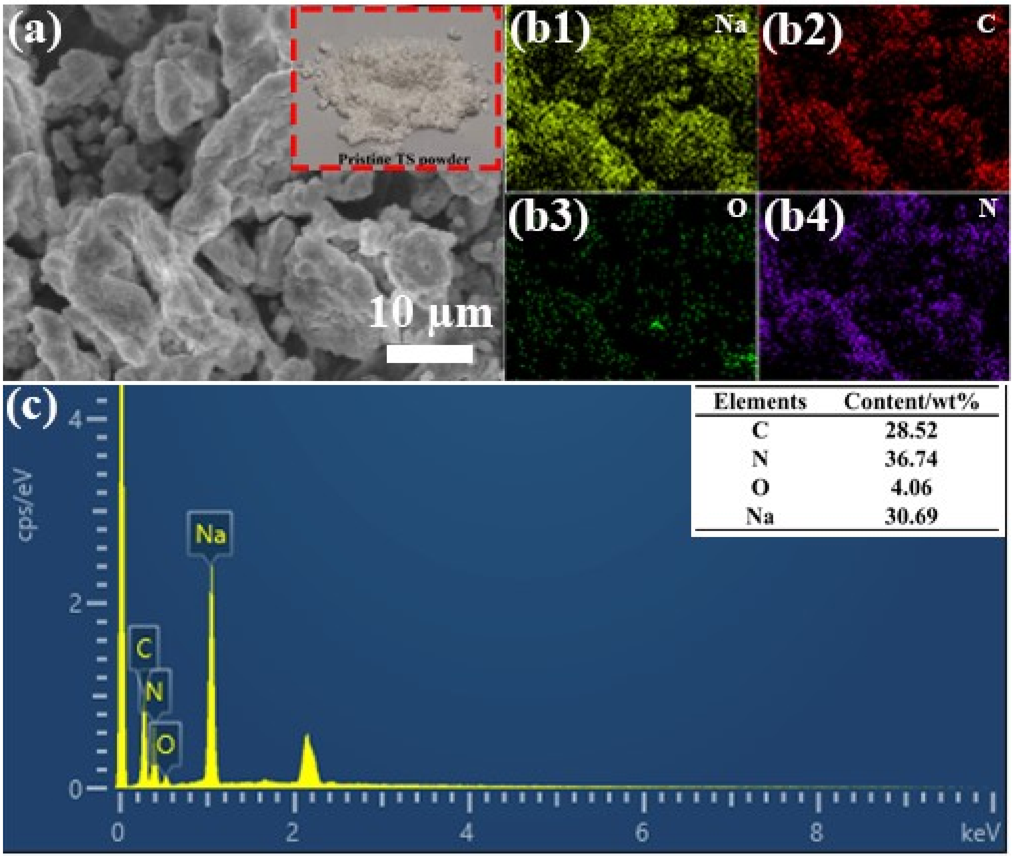

Elements	Content/wt%
C	28.52
N	36.74
O	4.06
Na	30.69

Fig. S2. (a) SEM images (inset is the optical photo of pristine TS powder), (b) the corresponding elemental mapping images and (c) EDX spectrum of pristine TS powder.

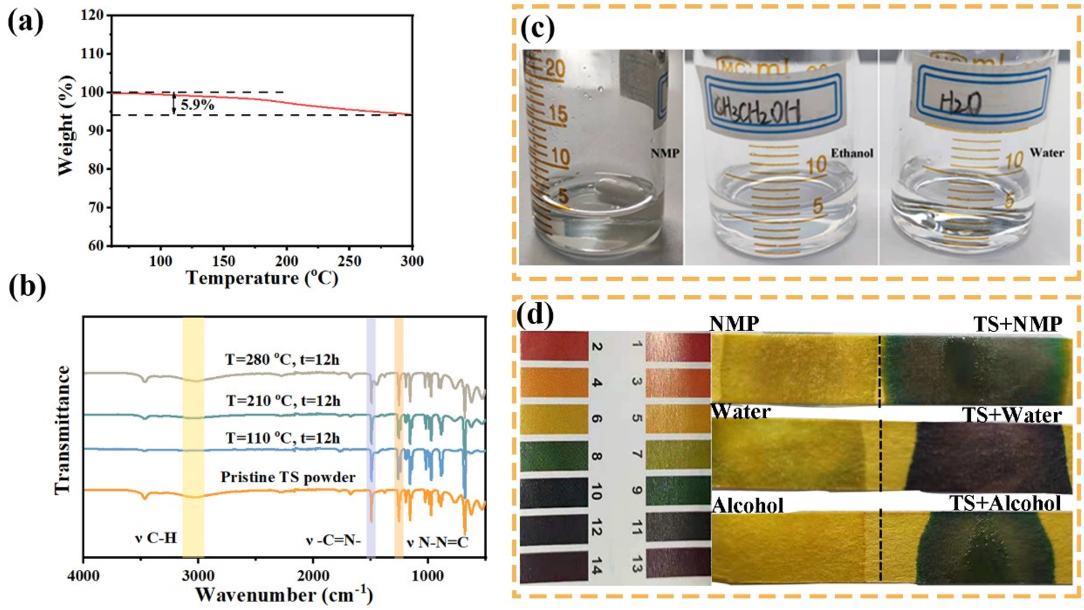

Fig. S3. (a) TG curve of pristine TS powder. (b) FTIR spectra of TS powder dried at different temperatures. (c) Optical photos of TS dissolved in different solvents (NMP, water, and alcohol) and (d) the corresponding pH testing.

In **Fig. S3a**, the thermogravimetric analysis curve demonstrates slight weight loss (~5.9%) within 300 °C in Ar atmosphere, indicating the thermal stability of TS. Meanwhile, FTIR spectra of the dried TS samples show no difference from that of the pristine TS, in which these adsorption peaks at 3022 cm^{-1}, 1455 cm^{-1} and 1247 cm^{-1} are indexed to the vibration of C-H, -C=N- and N-N=C in TS molecular, respectively (**Fig. S3b**).[1] TS also shows good solubility in NMP, water and alcohol (**Fig. S3c** and **Table S1)**, beneficial for the uniform distribution of cathode additive in the electrode. Besides, these TS solutions all show alkaline (**Fig. S3d**).

Table S1. The solubility of TS powder in different solvents

Solvent	Solubility/mg mL^{-1}
NMP	~25
Alcohol	~25
Water	>200

Note: the value of solubility provided in this work is rough and for reference only.

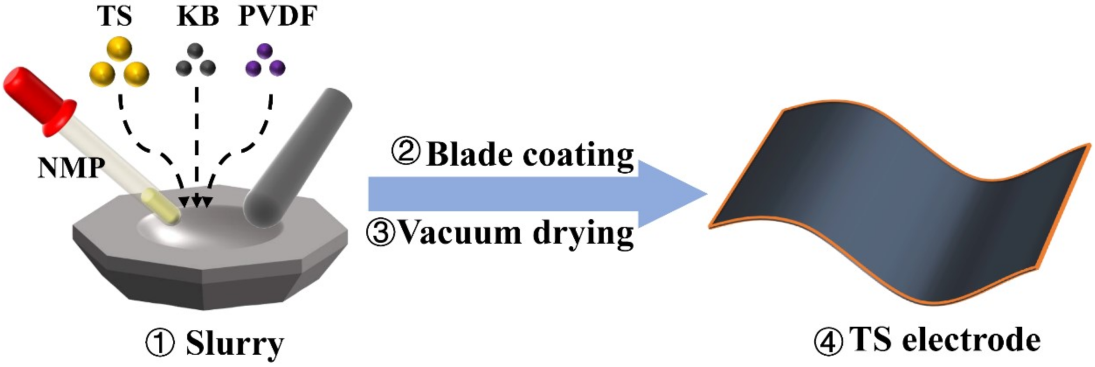

Fig. S4. The illustration of the preparation process of TS electrode.

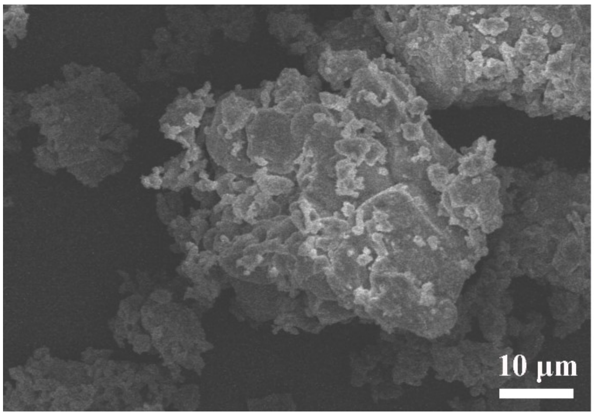

Fig. S5. (a) SEM image of the commercial Na_2CO_3 powder.

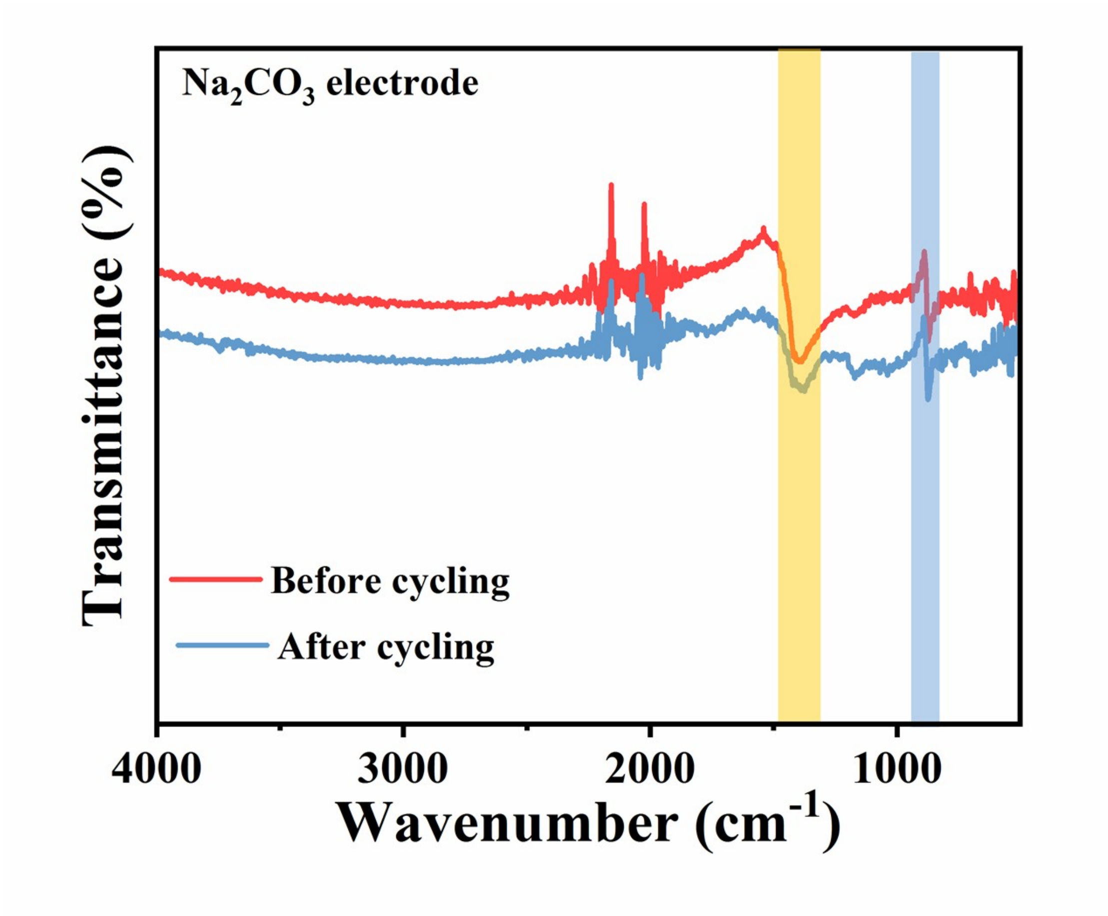

Fig. S6. FTIR spectra of Na_2CO_3 electrode before and after cycling.

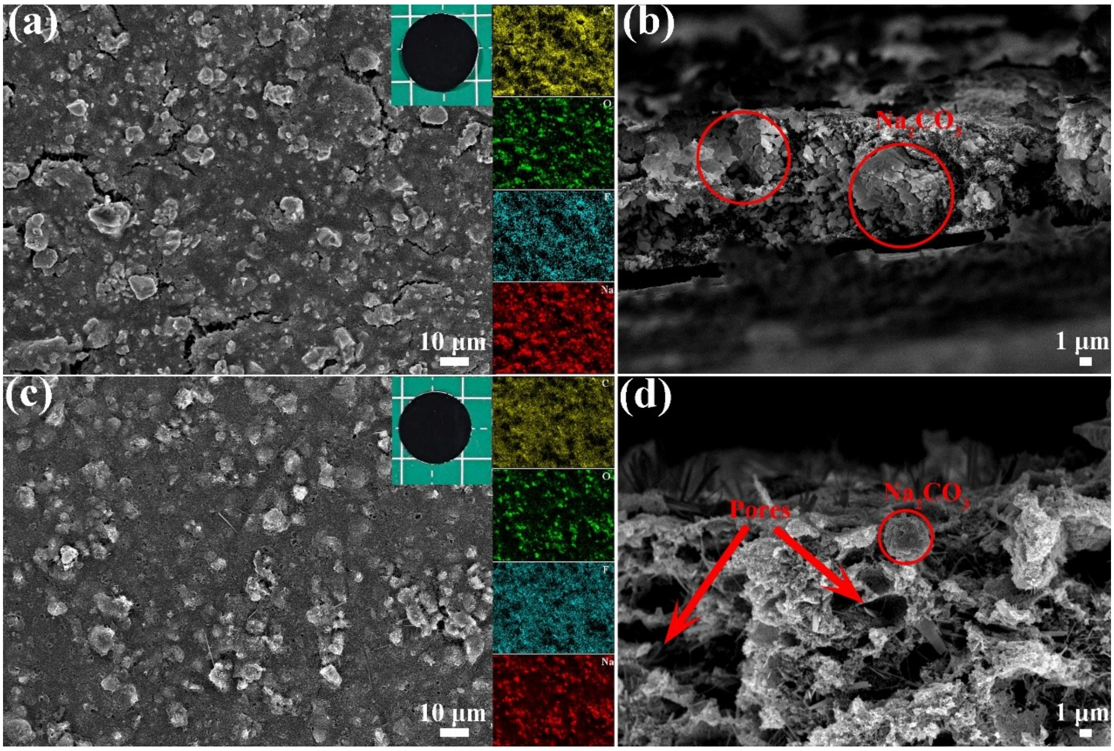

Fig. S7. (a) Surface SEM image and the corresponding elemental mapping image (the inset is the optical photo of electrode) and (b) Sectional SEM image of the fresh Na_2CO_3 electrode. (c) Surface SEM image and the corresponding elemental mapping image and (d) Sectional SEM image of the charged Na_2CO_3 electrode.

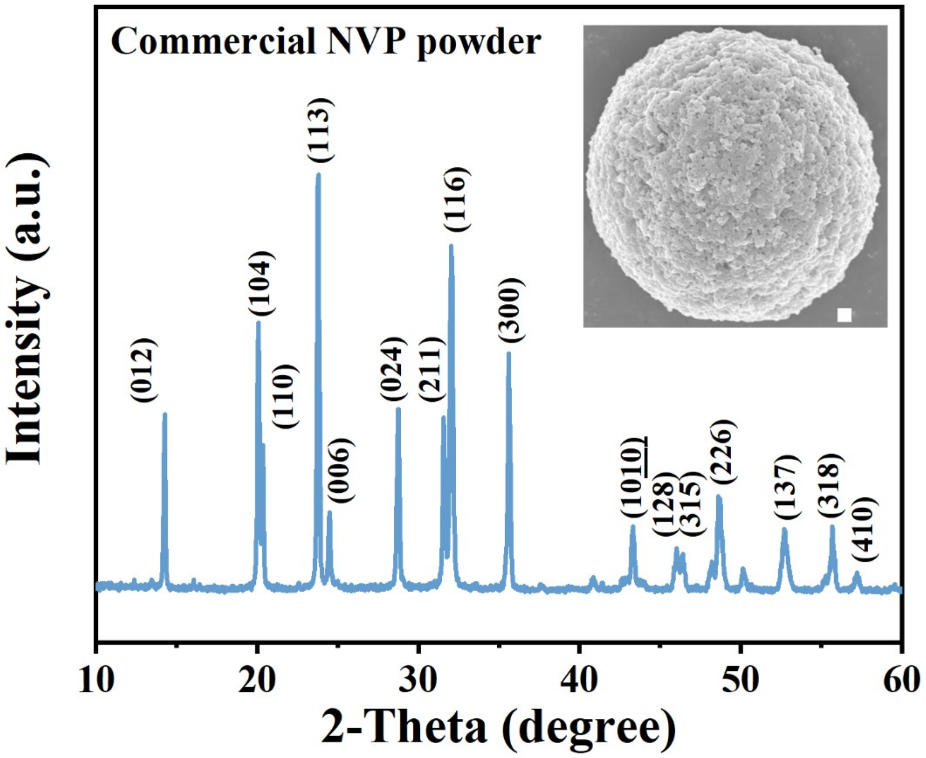

Fig. S8. XRD pattern of commercial NVP (the inset is SEM image with the scale bar of 1 μm).

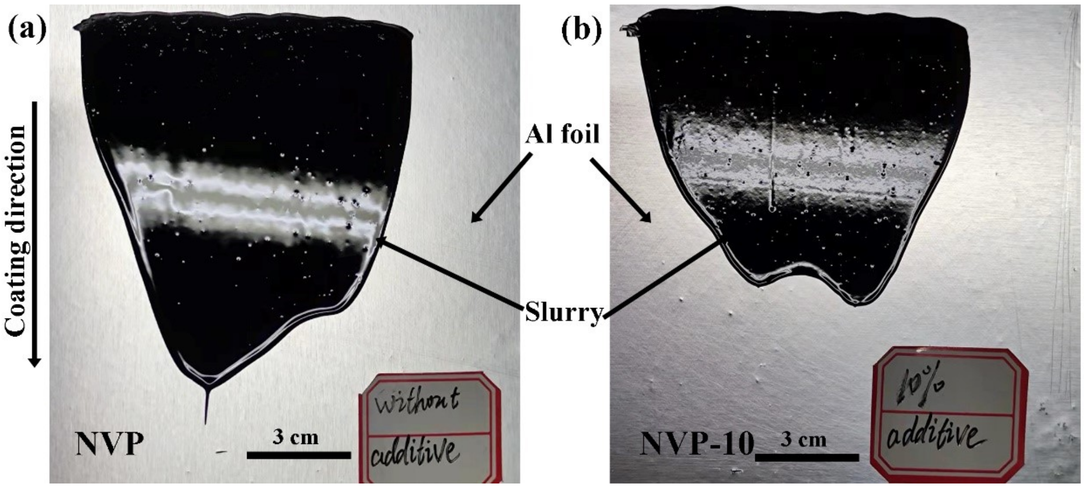

Fig. S9. Optical photos of the slurry just pasted on Al foil (without drying). (a) NVP electrode, (b) NVP-10 electrode.

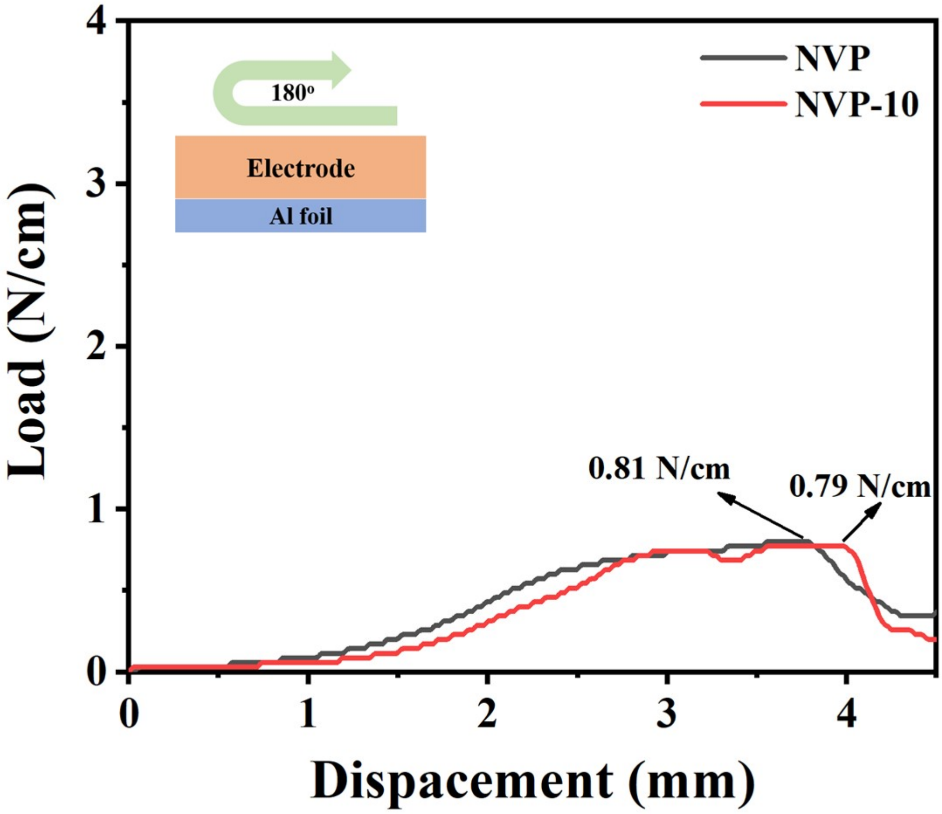

Fig. S10. 180^0 peeling test curves of NVP and NVP-10 electrode.

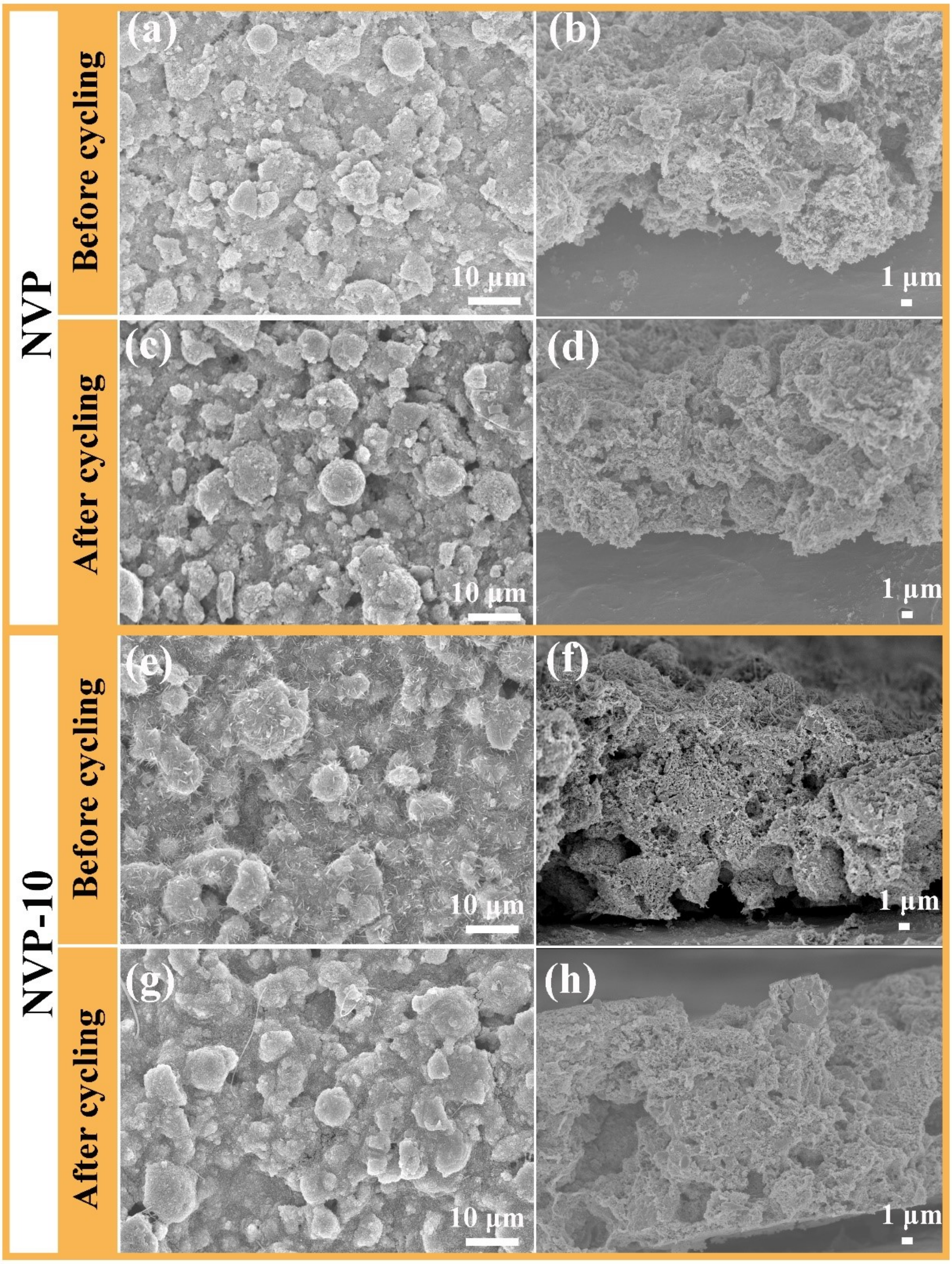

Fig. S11. (a) Surface SEM image and (b) sectional SEM image of NVP electrode before cycling. (c) Surface SEM image and (d) sectional SEM image of NVP electrode after cycling. (e) Surface SEM image and (f) sectional SEM image of NVP-10 electrode before cycling. (g) Surface SEM image and (h) sectional SEM image of NVP-10 electrode after cycling.

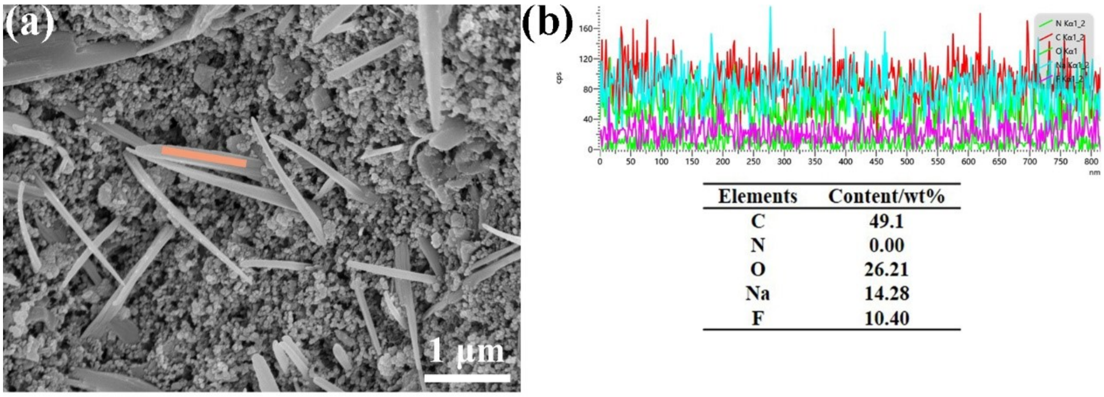

Elements	Content/wt%
C	49.1
N	0.00
O	26.21
Na	14.28
F	10.40

Fig. S12. (a) The enlarged SEM image of NVP-10 electrode. (b) Linear EDX spectrum of nanobelt marked with orange rectangle.

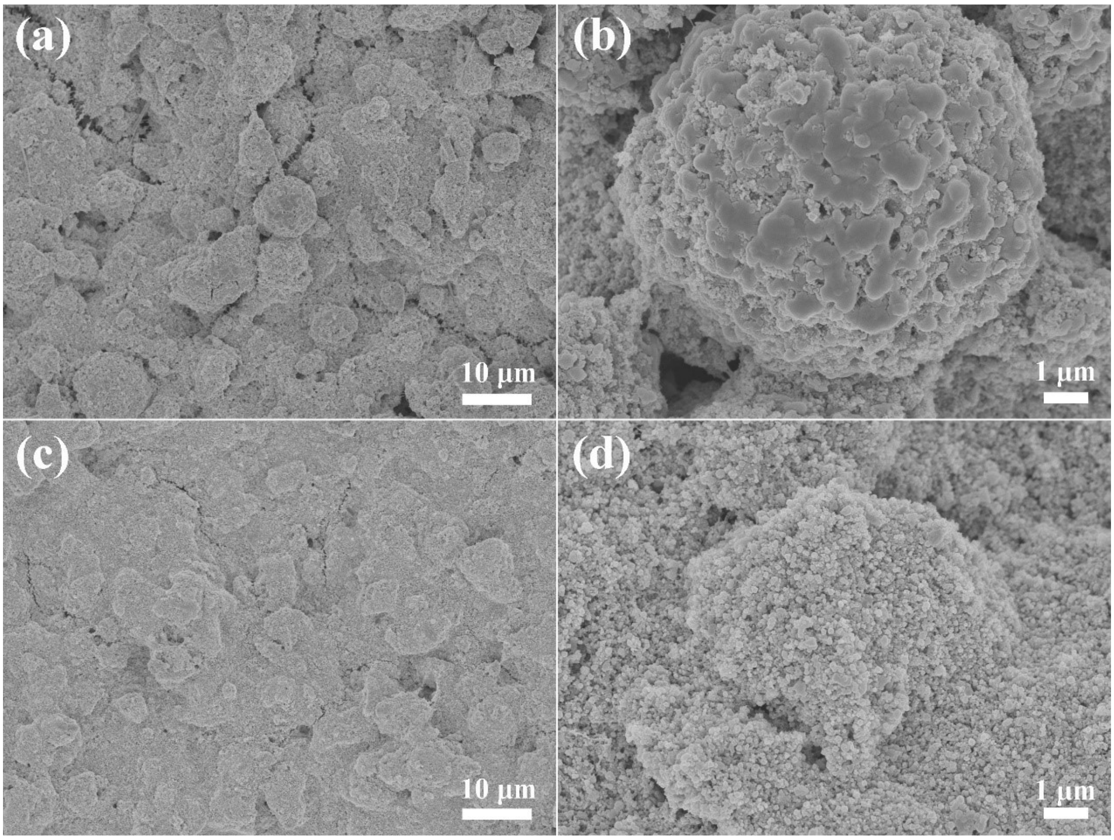

Fig. S13. SEM images of electrode after 100 cycles at 50 mA g^{-1}. (a, b) NVP, (c, d) NVP-10.

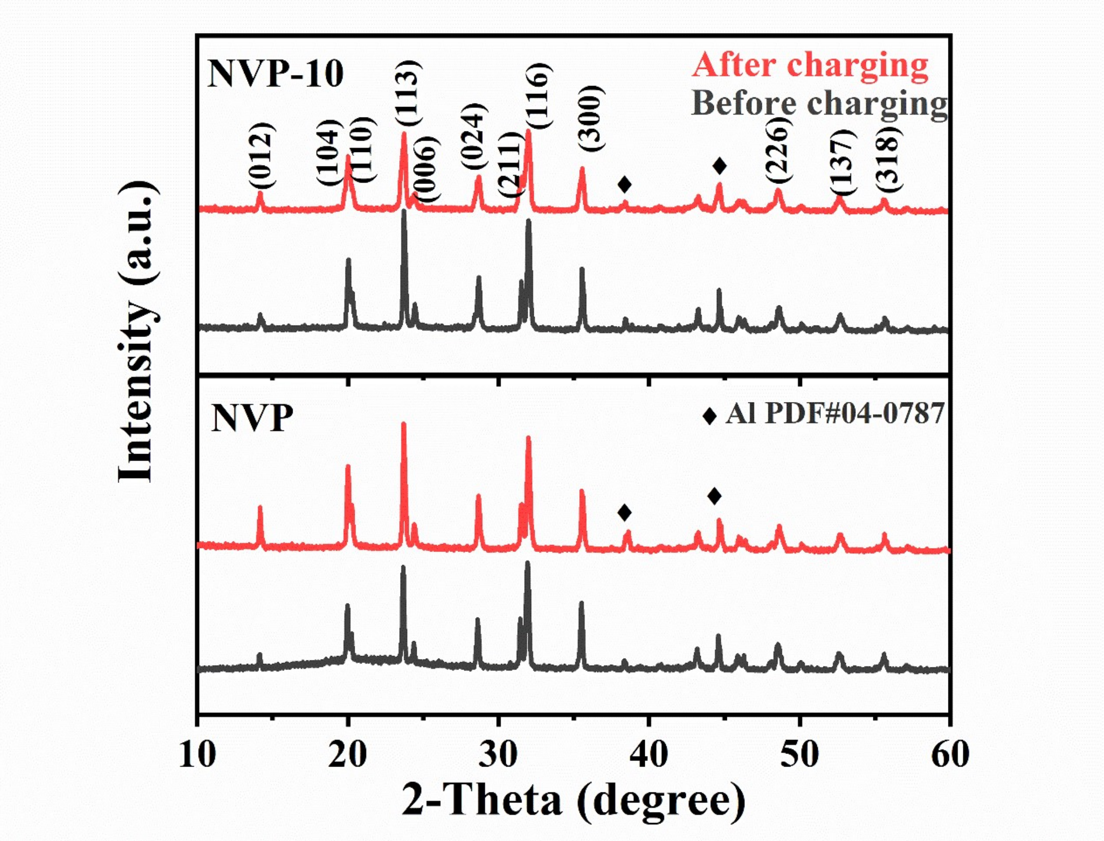

Fig. S14. XRD patterns of NVP and NVP-10 electrodes before and after cycling.

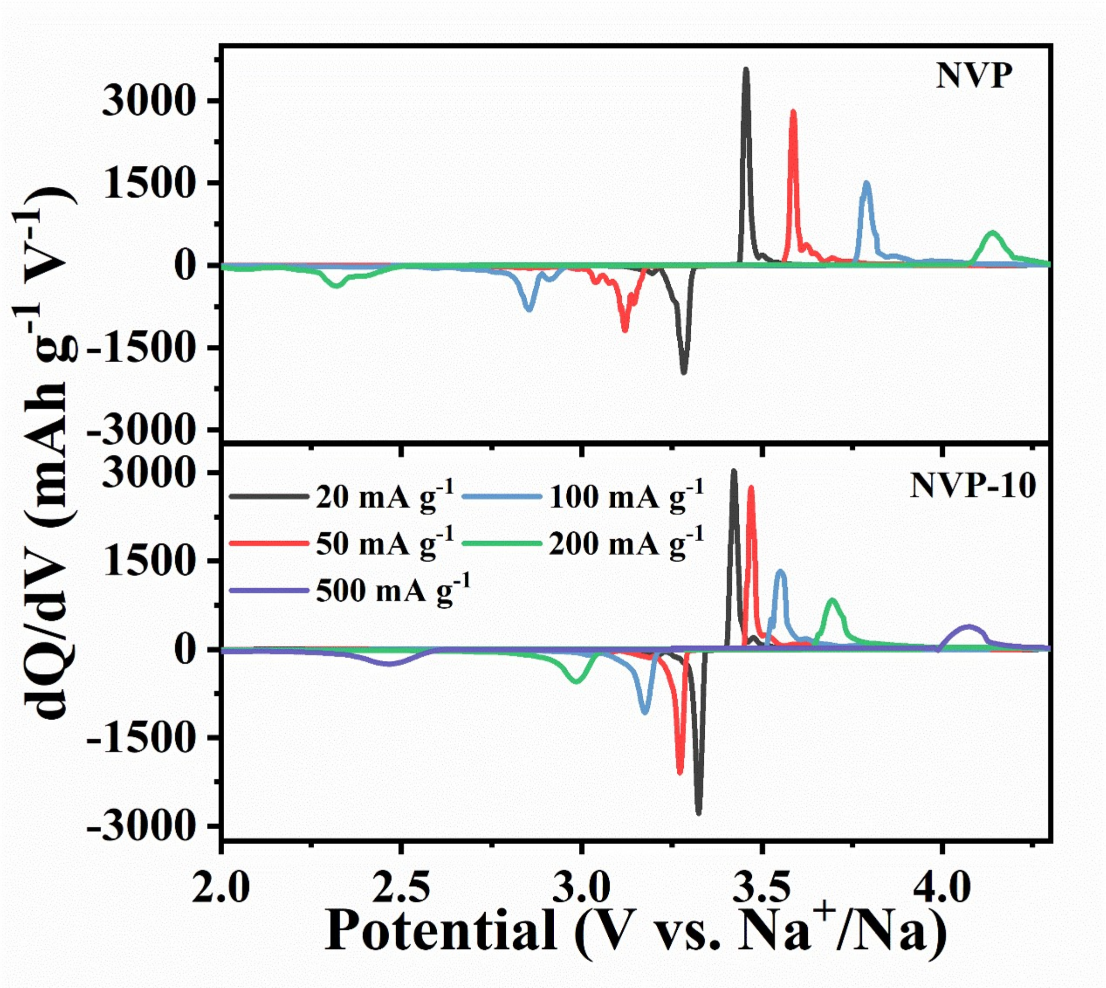

Fig. S15. dQ/dV curves based on charge/discharge curves shown in **Fig 2g**.

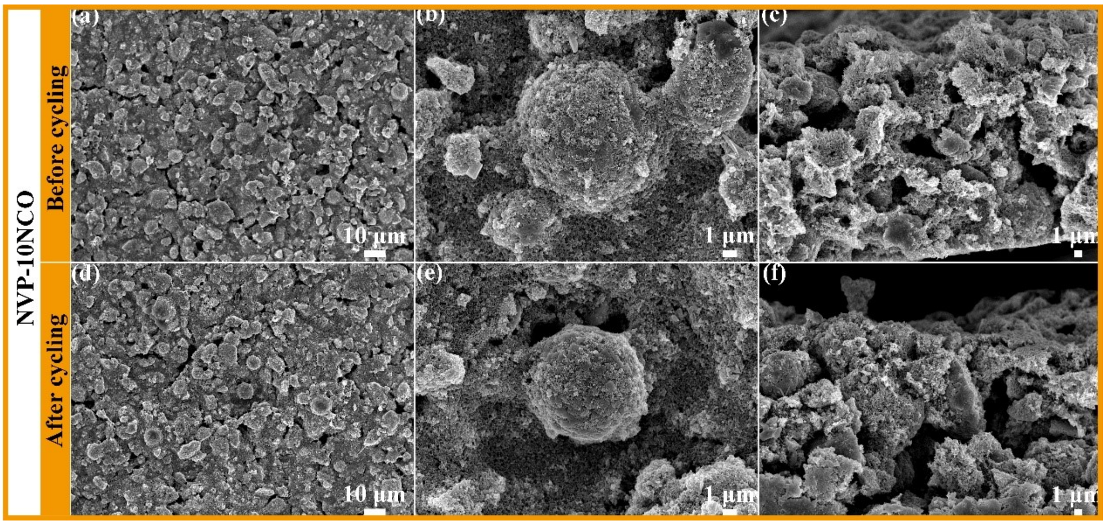

Fig. S16. (a, b) Surface SEM images and sectional SEM image of NVP-10NCO before cycling. (d ,e) Surface SEM images and sectional SEM image of NVP-10NCO after cycling.

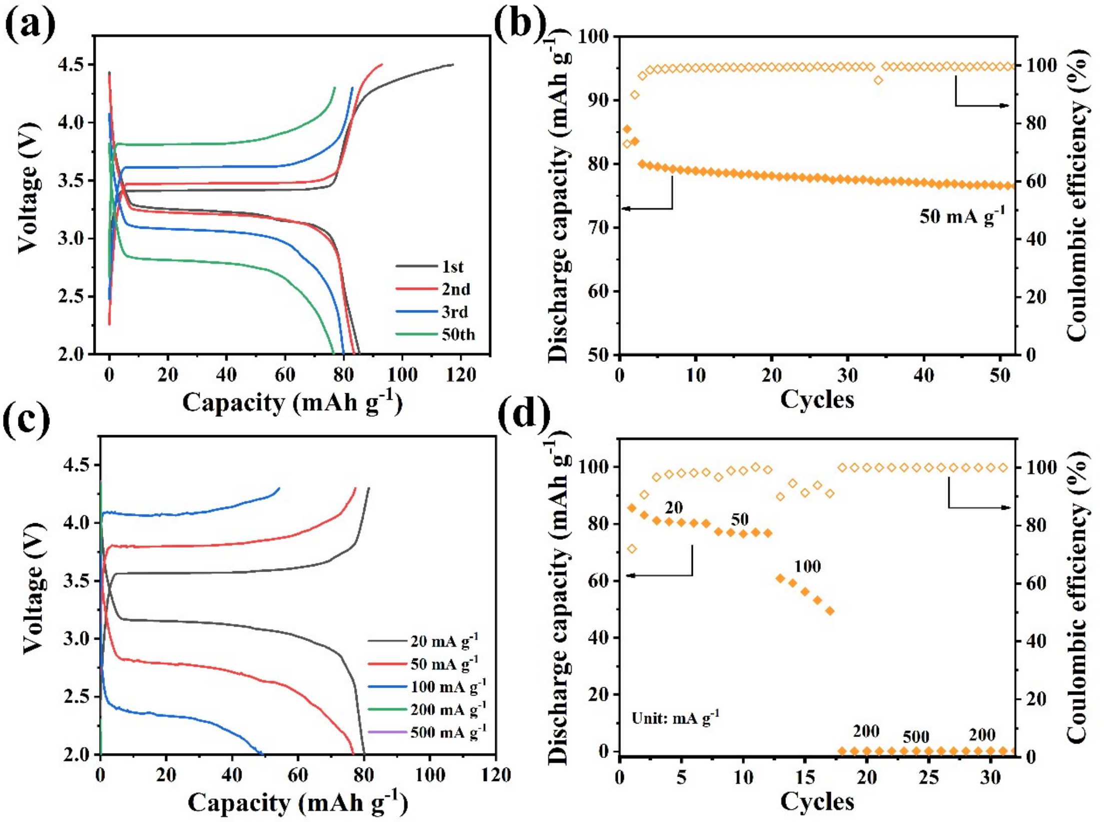

Fig. S17. (a) Electrochemical performance comparison of NVP-10NCO based on the total mass of fresh electrode: (a) galvanostatic charge/discharge curves at different cycles, (b) cycling performance, (c) galvanostatic charge/discharge curves at different current densities, (d) rate performance.

In **Fig. S17a**, the first charge/discharge capacity of NVP-10NCO is 117 and 86 mAh g^{-1}. Although NVP-10NCO shows the satisfactory cycling stability with a capacity retention of 96% after 50 cycles at 50 mA g^{-1} in **Fig. S17b**, the overpotential of electrode increases rapidly from 0.55 V to 0.95 V. Moreover, the capacity of NVP-10NCO is reduced with the increasing current density, which should be ascribed to the huge overpotential and the increased internal resistance.

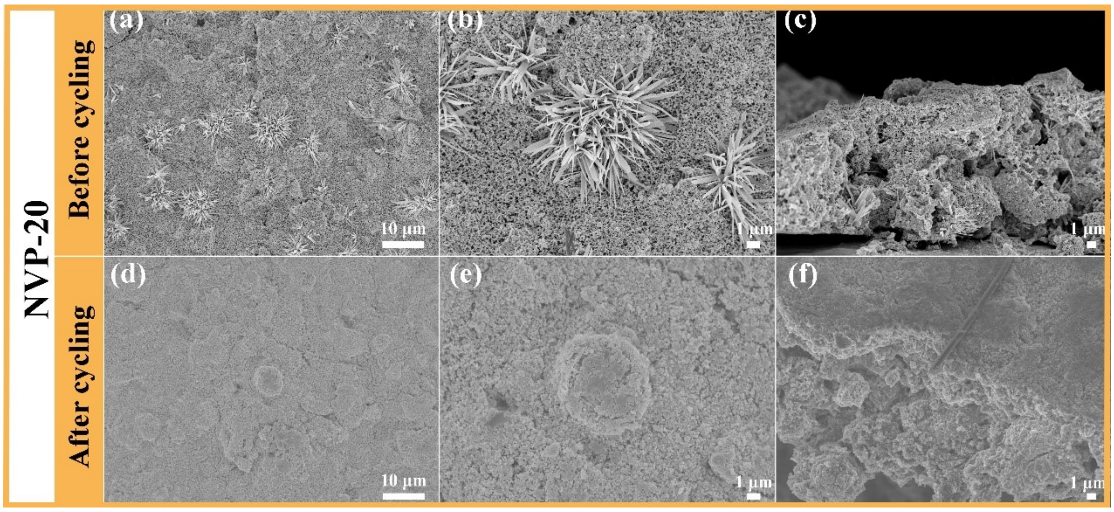

Fig. S18. (a,b) Surface SEM image and (c) sectional SEM image of NVP-20 electrode before cycling. (d,e) Surface SEM image and (f) sectional SEM image of NVP-20 electrode after cycling.

Alike, the obtained NVP-20 with 20 wt% TS also shows compact surface morphology before and after charging except that TS derived needle-like crystals aggregate together to form flower-like structure which distribute unevenly on the surface of uncycled electrode (**Fig. S18**). Besides, some needle-like crystals are also found in the inner of NVP-20 before cycling, which also disappear after cycles.

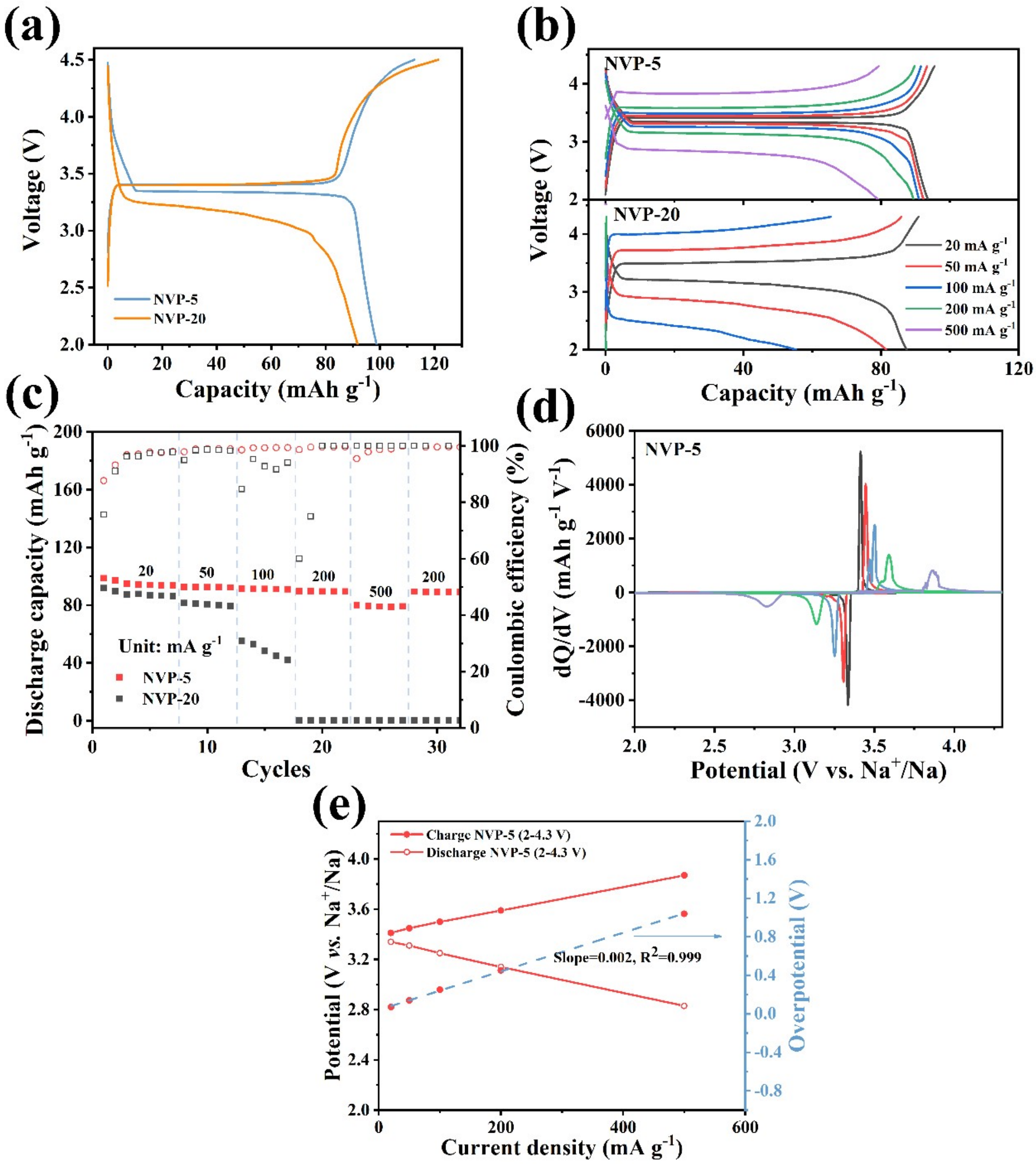

Fig. S19. (a) The first galvanostatic charge/discharge curves, (b) galvanostatic charge/discharge curves at different current densities, (c) rate performance of NVP-5 and NVP-20. (d) dQ/dV curves and (e) separation (polarization) between the cathodic and anodic peaks in the dQ/dV curves as a function of current density for NVP-5.

Similar to NVP-10, the first charge capacities NVP-5 and NVP-20 increase to 113 and 121 mAh g^{-1} owing to the decomposition of additive, respectively (**Fig. S19a**). Although the excess TS additive can compensate more irreversible capacity loss, NVP-20 undergoes serious polarization process and rapid capacity degradation along with the increased current density (**Fig. 19b** and **c**). When the amount of TS additive is reduced to 5 wt%, NVP-5 delivers the same capacity as NVP-10 at different rates and also remains a capacity of 79 mAh g^{-1} at 500 mA g^{-1}. Nevertheless, the slope of linear fitting equation for NVP-5 (R^2=0.999), which represents the growth rate of polarization, is only 0.002, demonstrating better rate capability in contrast with NVP-10 (**Fig. S19e**). To balance the sodium compensation capacity and the operation voltage, the optimized amount of TS in the slurry is 10 wt%.

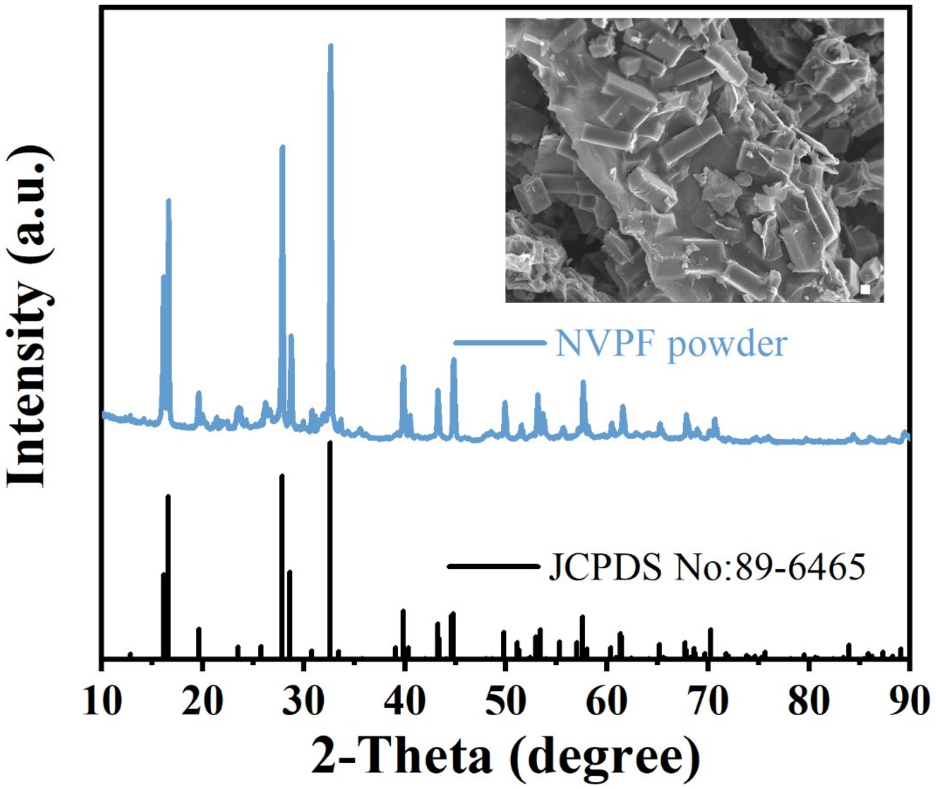

Fig. S20. XRD pattern of as-prepared NVPF (the inset is SEM image with the scale bar of 1 μm).

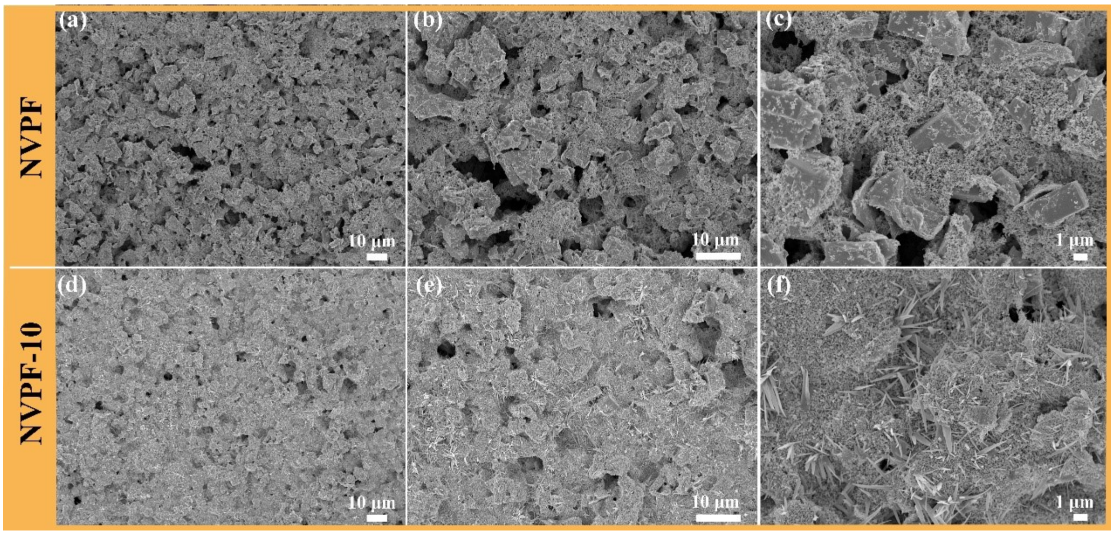

Fig. S21. SEM images of (a-c) NVPF and (d-f) NVPF-10.

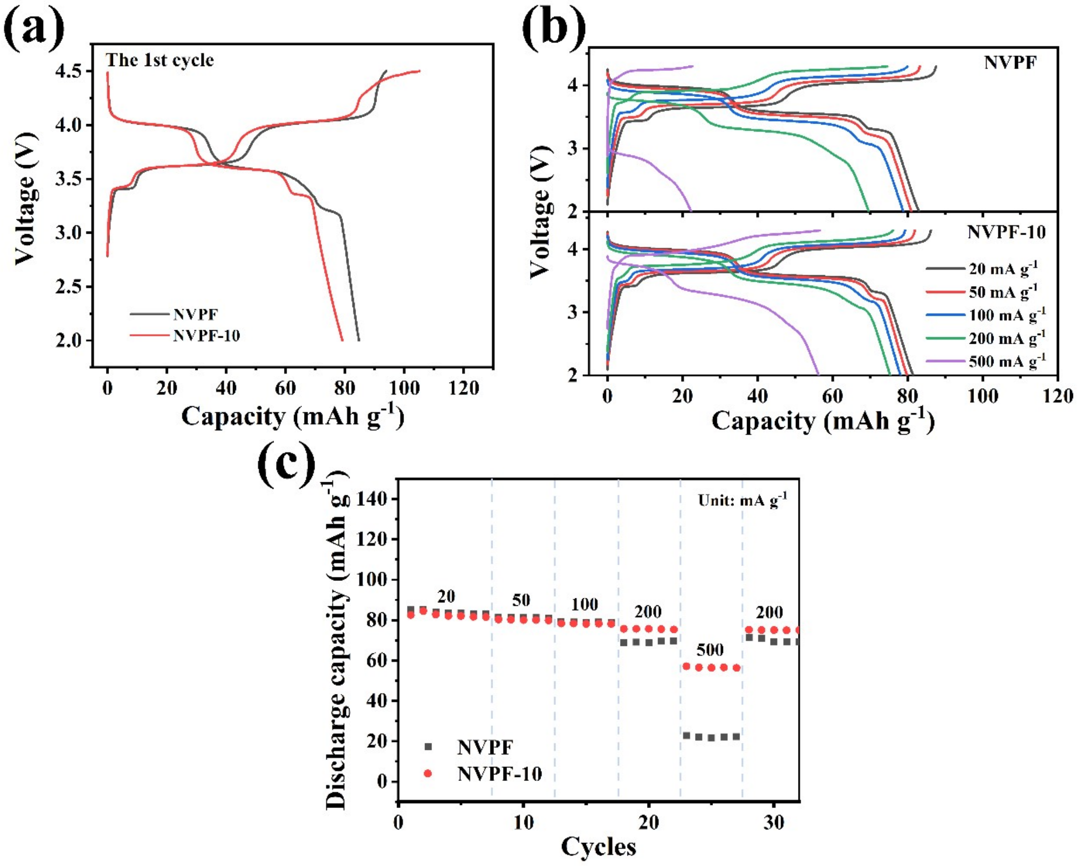

Fig. S22. (a) The first charge/discharge curves, (b) charge/discharge curves at different current densities and (c) rate performance of NVPF and NVPF-10 electrodes.

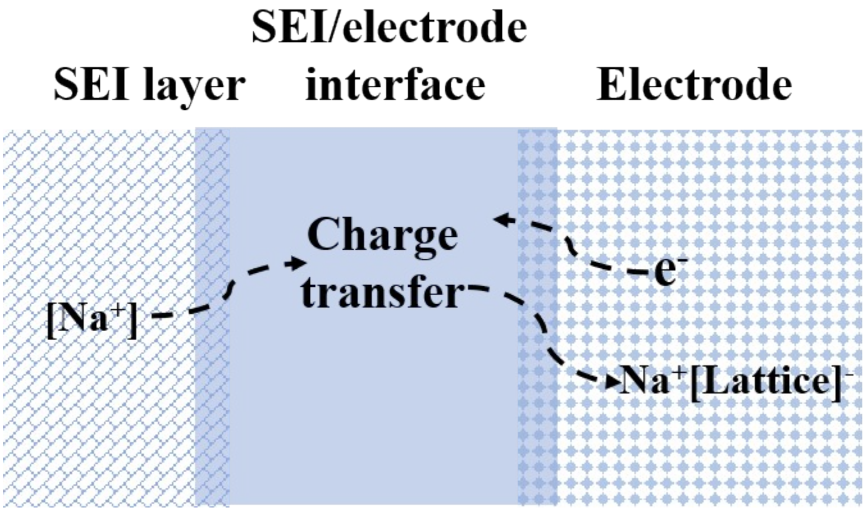

Fig. S23. Schematic of the sodiation process of electrode. [Na^+] means that the Na^+ may be solvated.

Table S2. Resistance data obtained from the fitting impedance spectra

	R_e/ohm	R_f/ohm	R_{ct}/ohm
NVP after 2 cycles	3.6	160.6	2553
NVP after 10 cycles	4.3	179.5	3829
NVP-10 after 2 cycles	12.8	273.6	751.1
NVP-10 after 10 cycles	7.20	372.9	913.6

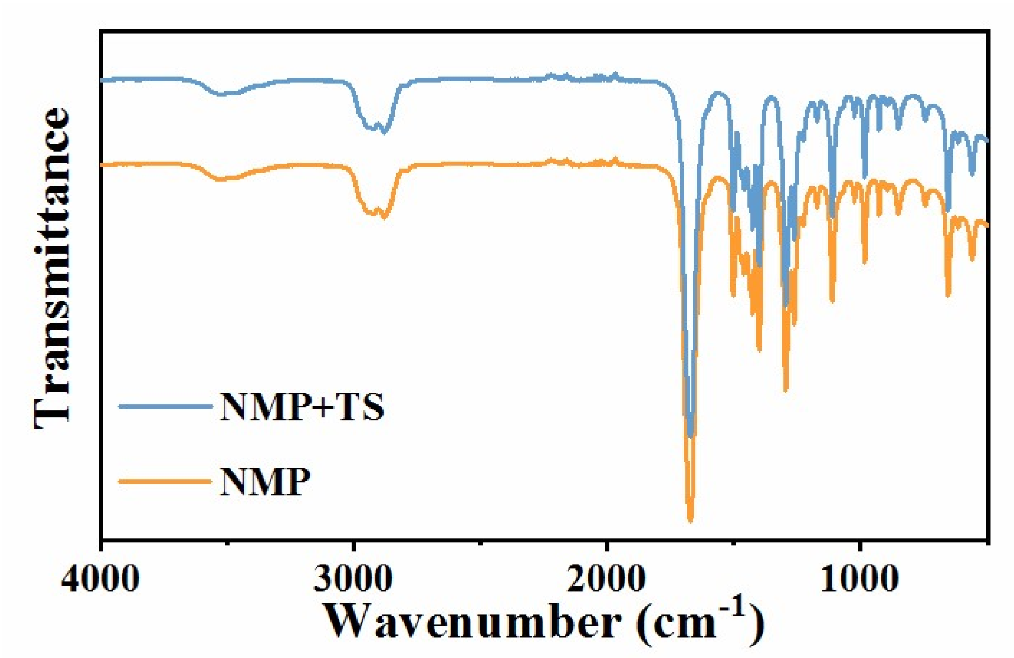

Fig. S24. FTIR sepctra of NMP and the solution with TS dissolved in NMP.

Considering the chemical stability of KB and the thermal stability of TS, the conversion of TS to Na_2CO_3 should have no concern with the introduction of KB and the simple vacuum-drying treatment. **Fig. S24** shows FTIR spectra of NMP solvent before and after adding TS, no obvious difference is found, indicating the chemical stability of TS dissolved in NMP at room temperature. Nevertheless, after evaporating TS solution in a vacuum drying oven, the recrystallized powder noted as R-TS-NMP is distinguished from the pristine TS. The characteristic peak indexed to -C=N- (1455 cm^{-1}) almost disappear and the vibration peaks corresponded to CO_3^{2-} are observed in FTIR spectrum of R-TS-NMP (**Fig. S25**).[1, 2] XRD pattern of R-TS-NMP also confirms the existence of Na_2CO_3 (**Fig. S26**). On basis of EDX spectrum in **Fig. S27**, the contents of N and O are 0 wt% and 38.2 wt%, respectively. Alike, the recrystallized samples (R-TS-water and R-TS-alcohol) were also obtained in water solution and alcohol solution for further investigation. R-TS-water and R-TS-alcohol show similar FTIR spectra and display strong vibration peak at ~1455 cm^{-1} in contrast to R-TS-NMP, ascribed to the unchanged -C=N- bonds.[1] Thus, R-TS-water and R-TS-alcohol still remain high N content and low O content similar to TS (**Fig. S28**).

As reported in some studies, NMP can be hydrolyzed to 4-(methylamino) butanoate (MBA) and other derivative products in the alkaline aqueous solution.[3, 4] Besides, carboxyl or sodiated carboxyl group in organics can be removed under certain conditions, which is called the decarboxylic reaction in organic chemistry. For example, acetic acid can react with NaOH to generate Na_2CO_3 according to Reaction (1).

$$CH_3COOH + NaOH \xrightarrow{\Delta} CH_4\uparrow + Na_2CO_3 \qquad \text{Reaction (1)}$$

The similar decarboxylic reaction might take place in this work, and thus TS can transform into Na_2CO_3. In fact, the underlying mechanism is still unclear and more efforts are needed.

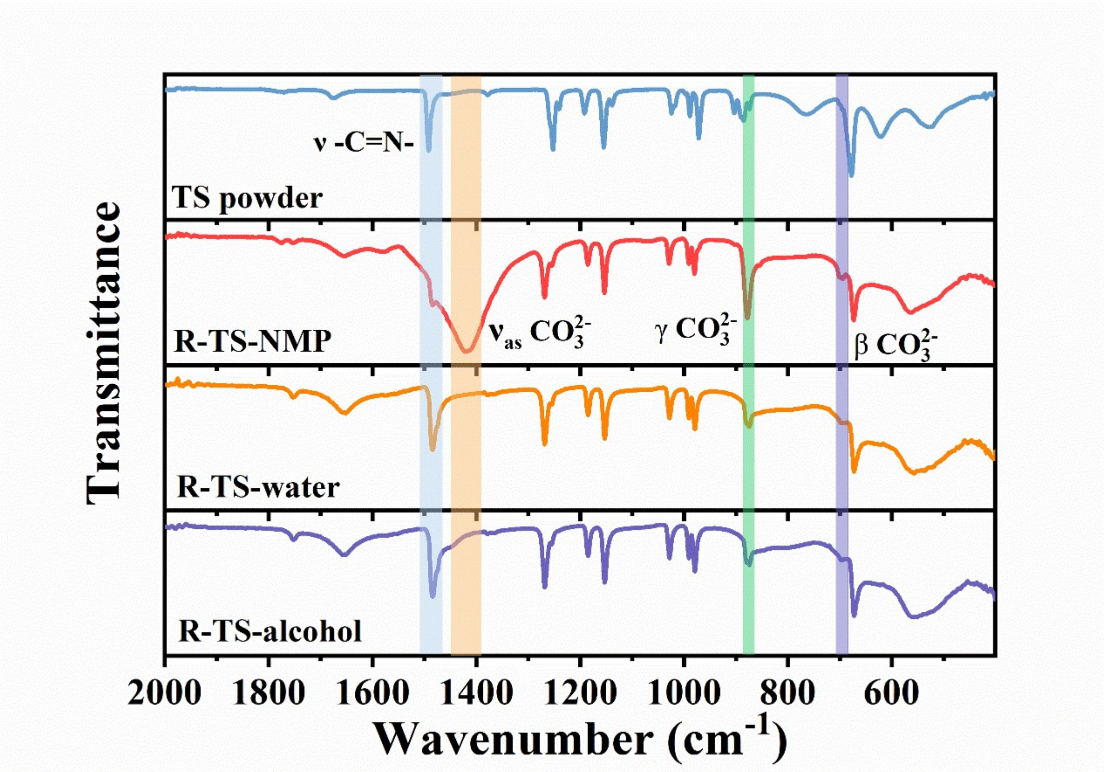

Fig. S25. FTIR spectra of R-TS-NMP, R-TS-water and R-TS-alcohol.

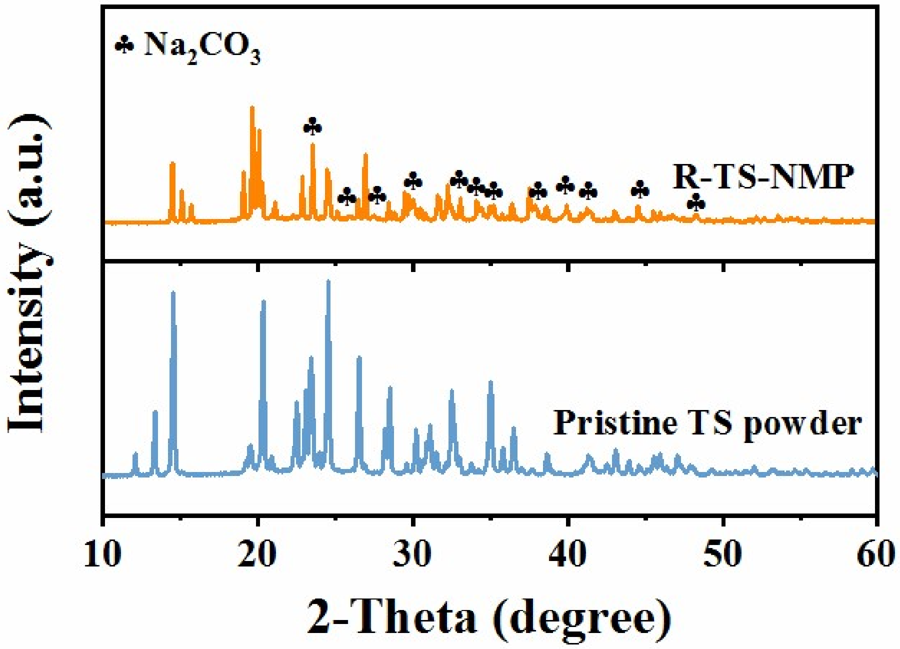

Fig. S26. XRD pattern of R-TS-NMP and pristine TS power

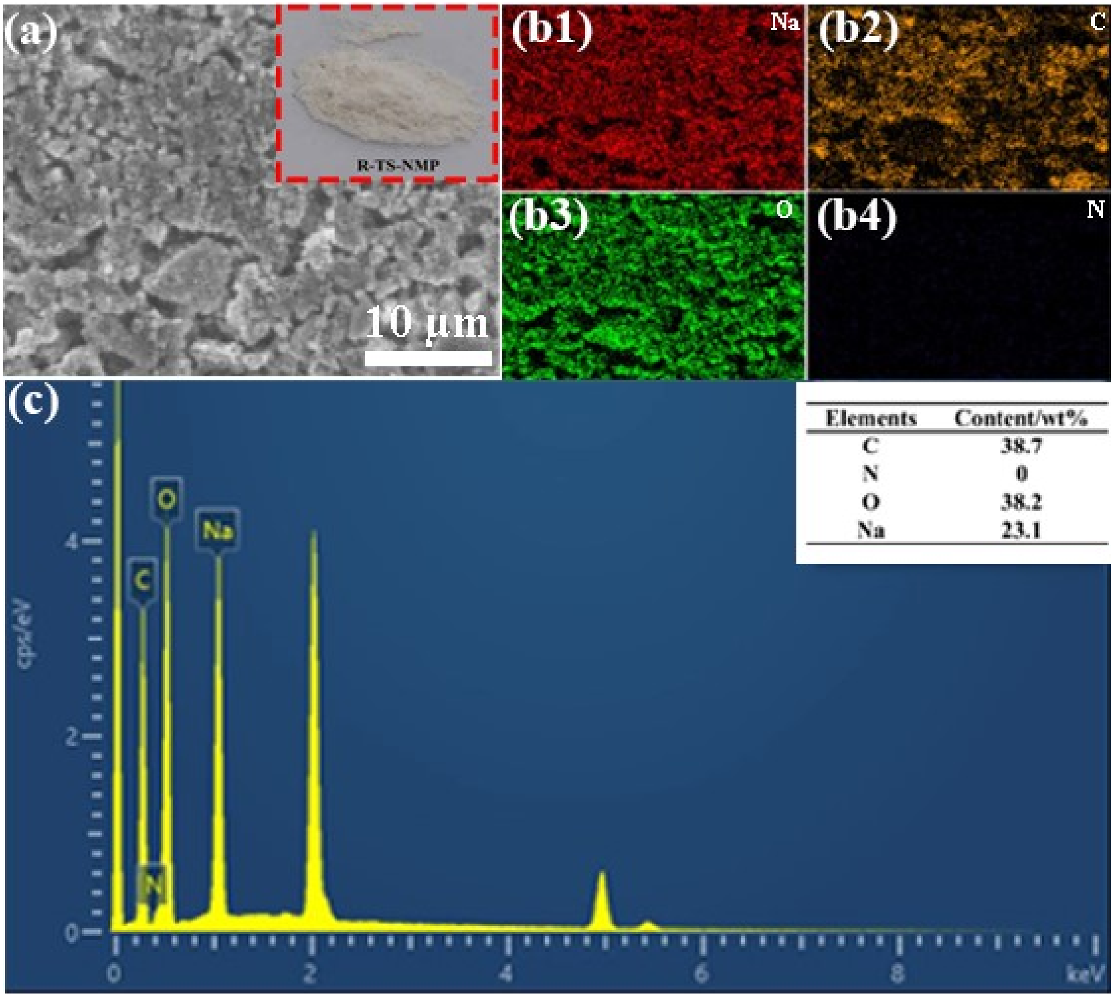

Elements	Content/wt%
C	38.7
N	0
O	38.2
Na	23.1

Fig. S27. (a) SEM image (inset is the optical photo of R-TS-NMP powder), (b) the corresponding elemental mapping image of R-TS-NMP and (c) EDX spectrum of R-TS-NMP.

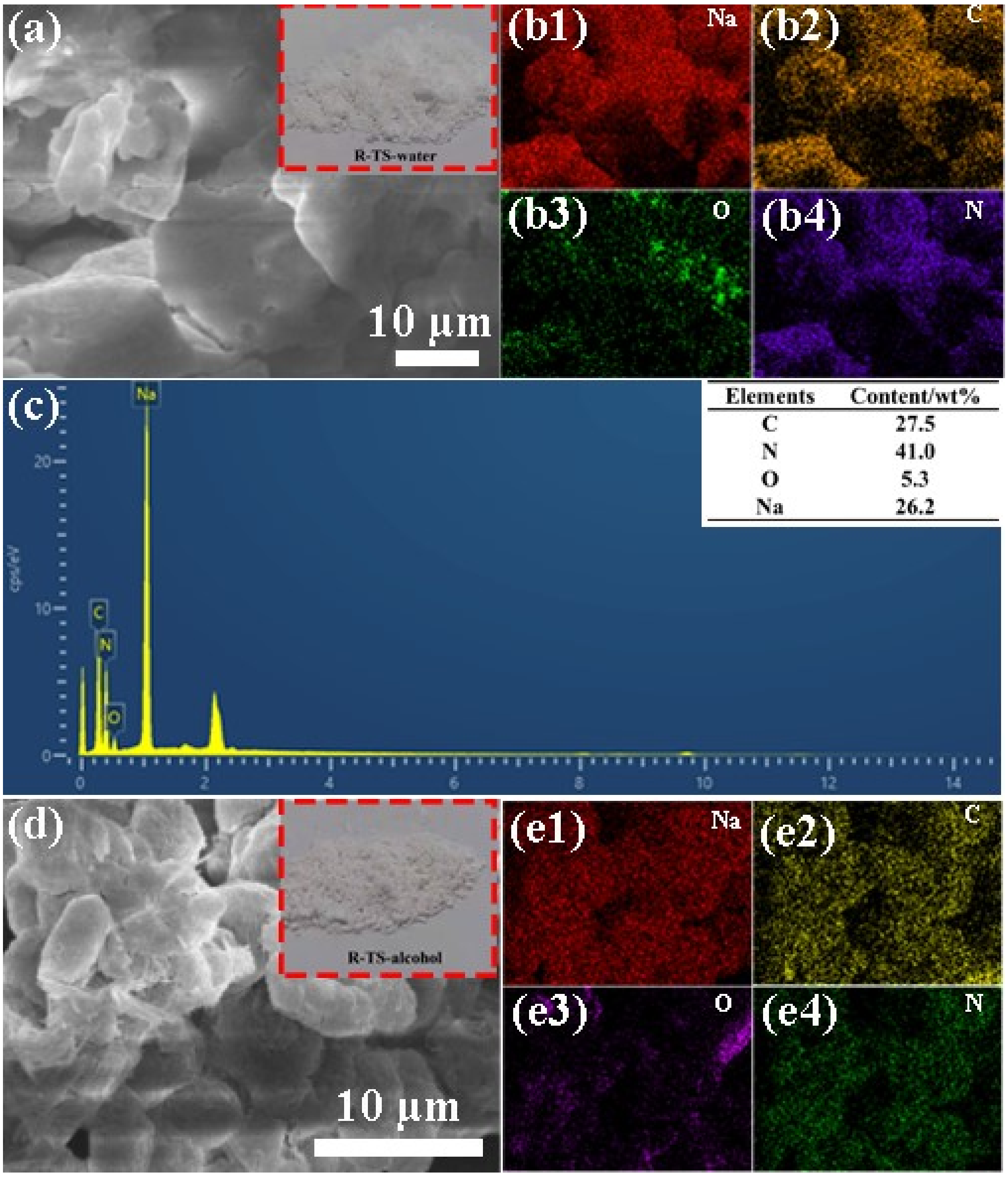

Elements	Content/wt%
C	27.5
N	41.0
O	5.3
Na	26.2

Fig. S28. (a) SEM image (inset is the optical image of R-TS-water powder), (b) elemental mapping image and (c) EDX spectrum of R-TS-water. (d) SEM image (inset is the optical image of R-TS-alcohol powder) and (e) elemental mapping image of R-TS-alcohiol.

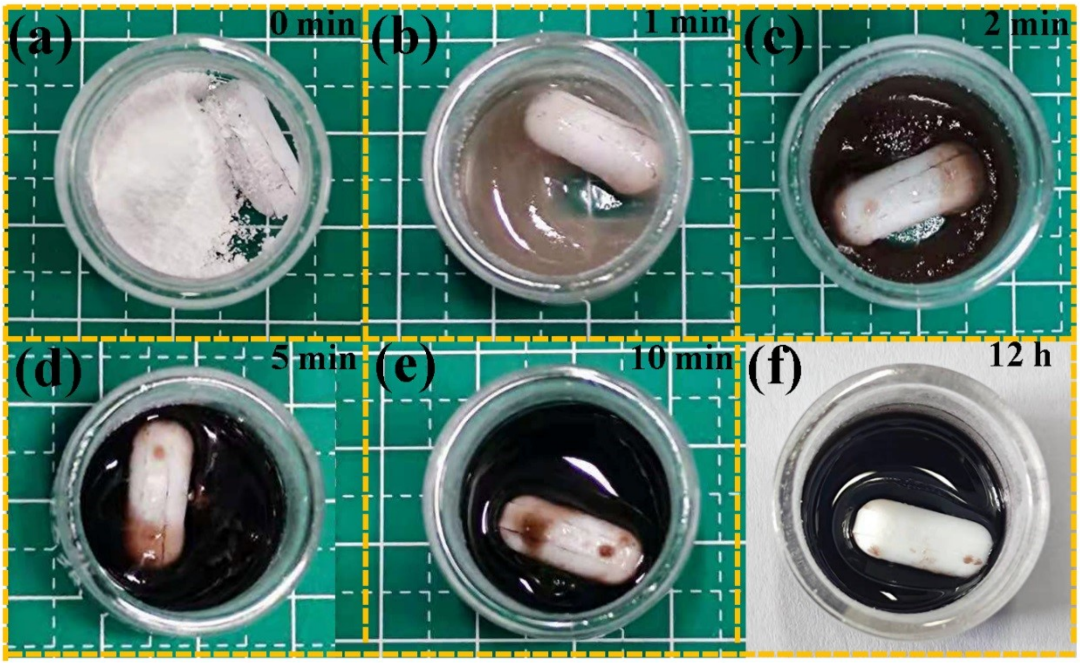

Fig. S29. Optical photos of slurry stirred for (a) 0 min, (b) 1 min, (c) 2 min, (d) 5 min, (e) 10 min and (f) 12 h.

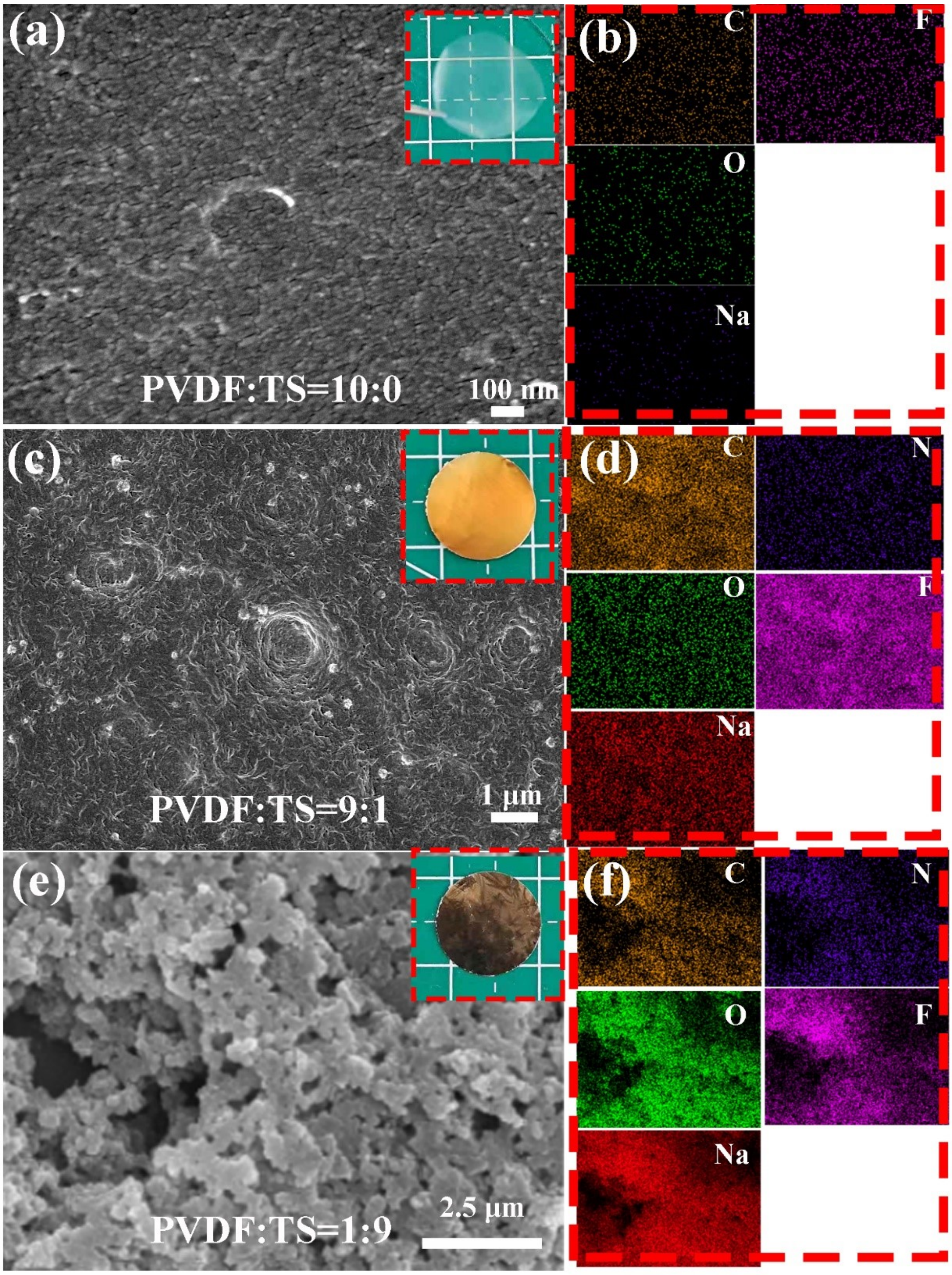

Fig. S30. SEM and the corresponding elemental mapping images of (a, b) P10T0, (c, d) P9T1, and (e, f) P1T9 (insets are optical images).

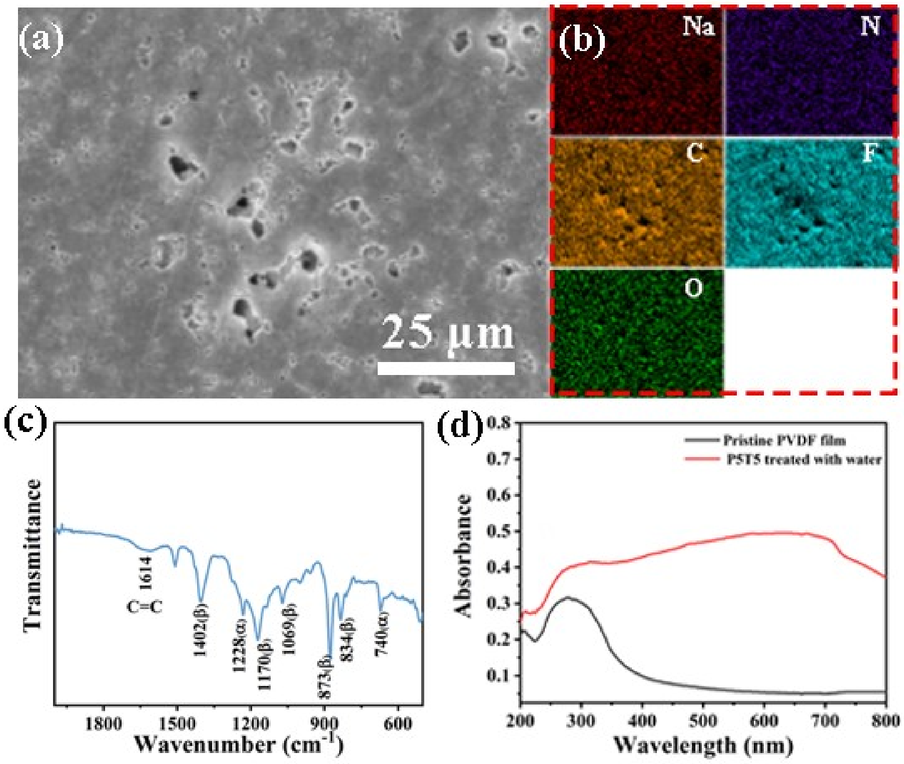

Fig. S31. (a) SEM image, (b) elemental mapping image and (c) FTIR spectrum of P5T5 film treated with water. (d) UV-vis spectra of pristine PVDF film and P5T5 treated with water.

Table S3. The contents of C, N, O, F and Na in P5T5 film treated with water

Elements	P5T5 film treated with water/wt%
C	45.5
N	6.7
O	3.2
F	44.3
Na	0.3

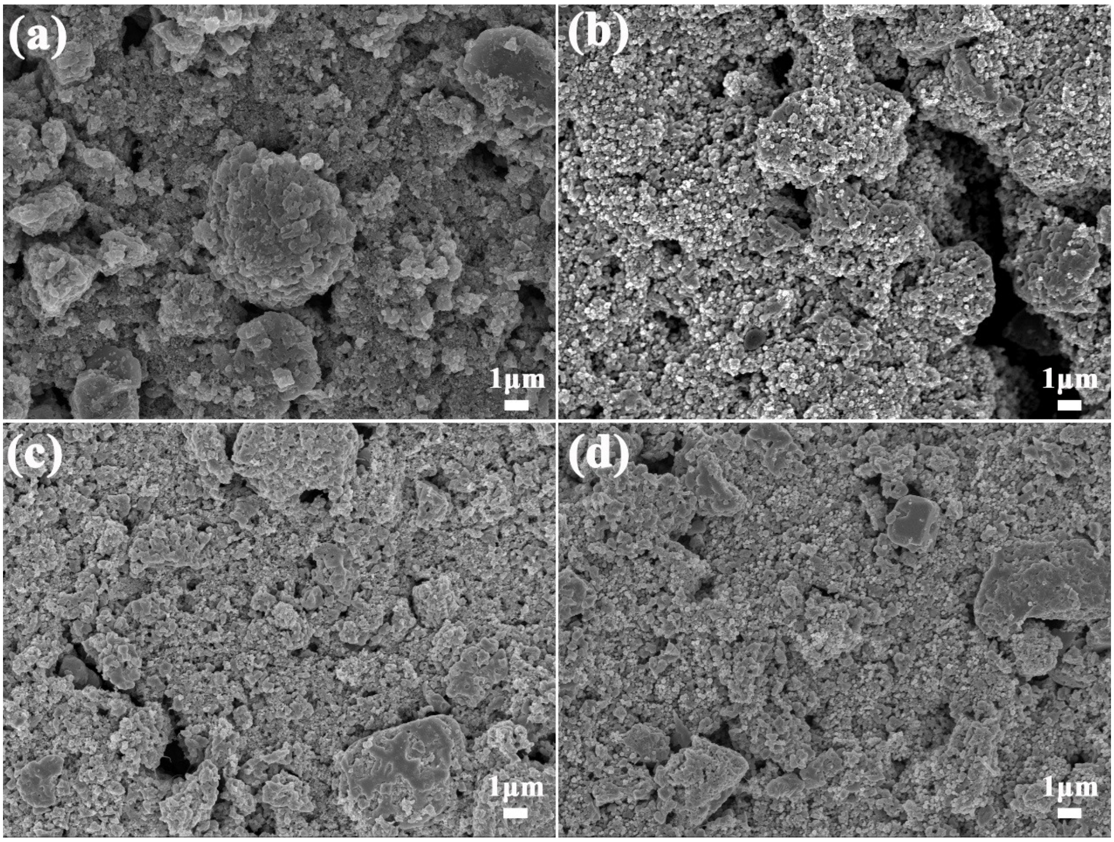

Fig. S32. SEM images. (a) NVP-SA before cycling. (b) NVP-SA after cycling. (c) NVP-SA-10 before cycling. (d) NVP-SA-10 after cycling.

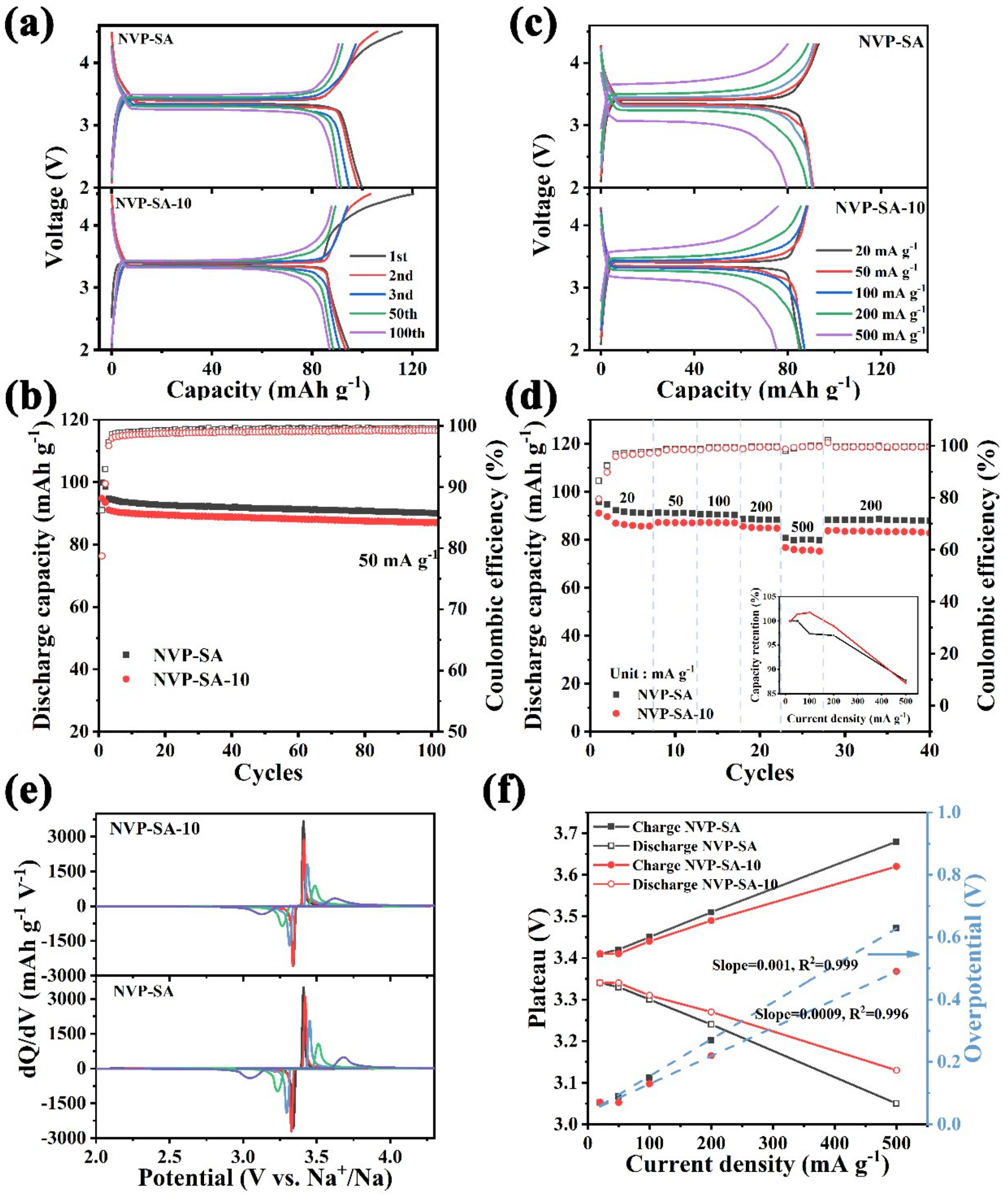

Fig. S33. Electrochemical performance based on the total mass of electrode. (a) Galvanostatic charge/discharge curves at different cycles, (b) cycling performance, (c) galvanostatic charge/discharge curves at different cycles, (d) rate performance, (e) dQ/dV curves and (f) separation (polarization) between the cathodic and anodic peaks in the dQ/dV curves as a function of current density for NVP-SA and NVP-SA-10 electrode.

The influence of TS additive on NVP electrode with aqueous binder was also explored, where fluorine-free sodium alginate was chosen. SEM images of NVP electrode with sodium alginate (NVP-SA) are shown in **Fig. S32a**, and there is loose contact between NVP cathode and KB carbon spheres, similar to the surface morphology of NVP electrode with PVDF binder. Differing from the distinct change in NVP-10 electrode, NVP-SA-10 electrode with 10 wt% TS added in the slurry remain the same morphology as NVP-SA, where no needle-like additive crystal is found owing to the absence of conversion reaction of TS and defluorination of PVDF (**Fig. S32c**). As shown in **Fig. 33a**, the initial charge capacities of NVP-SA and NVP-SA-10 are 115 mAh g^{-1} and 120 mAh g^{-1}, respectively. Besides, the first reversible discharge capacities of NVP-SA and NVP-SA-10 are 100 and 95 mAh g^{-1}, respectively. Even after 100 cycles at 50 mA g^{-1}, NVP-SA and NVP-SA-10 demonstrate discharge capacities of 90 mAh g^{-1} and 87 mAh g^{-1}, respectively, corresponding to the similar capacity retention of ~95% (**Fig. 33b**). The excellent cycling stability of NVP-SA and NVP-SA-10 electrodes is also confirmed by the unchanged electrode morphology (**Fig. S32b** and **Fig. S32d**). Actually, NVP-SA-10 shows less polarization increase after continuous cycles in contrast with NVP-SA, implying better cycling stability. The rate performance of NVP-SA-10 is also superior to that of NVP-SA and NVP-SA-10 (**Fig. S33d**). Moreover, the growth rate of polarization for NVP-SA electrode reduces from 0.001 to 0.0009 after adding TS additive (**Fig. S33e, f**).

Fig S34. Optical photo of Al current collector.

Fig. S35. Optical photos of (a) NVP electrode soaked in water for 24 h and (b) NVP-10 electrode soaked in alcohol for 24 h

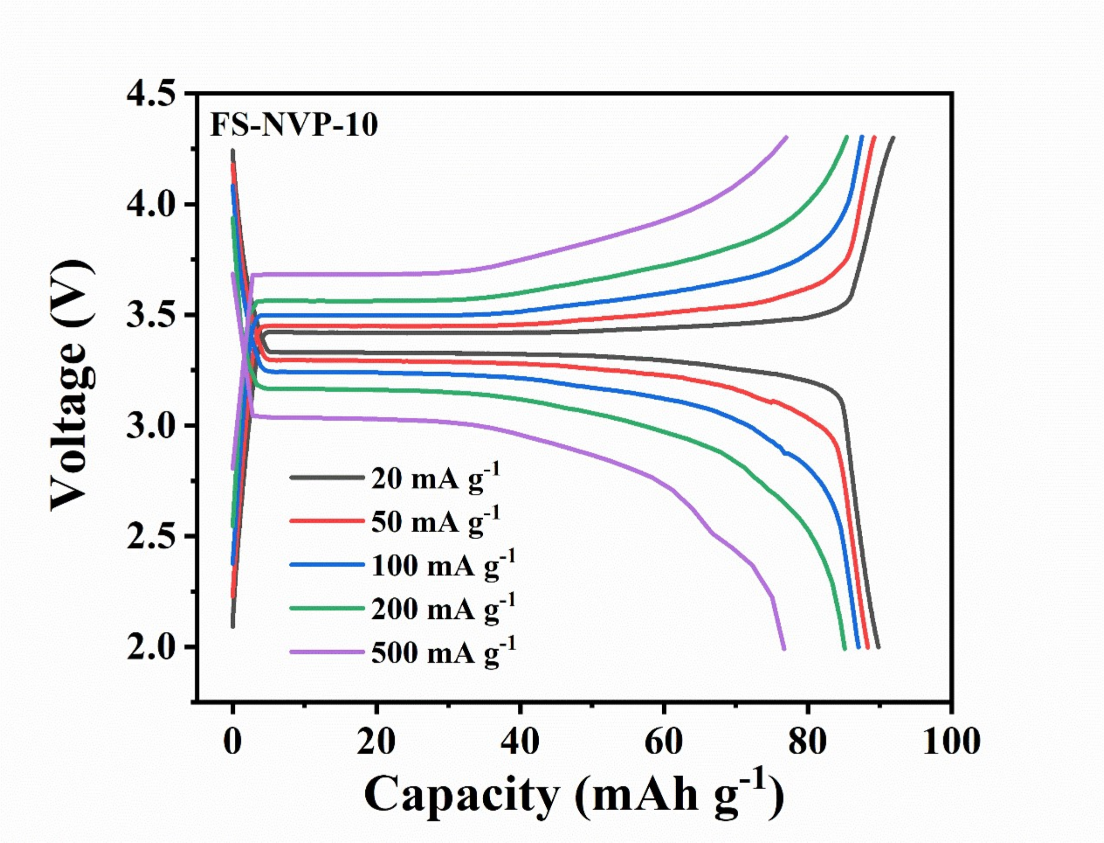

Fig. S36. Charge/discharge curves of FS-NVP-10 at different current densities.

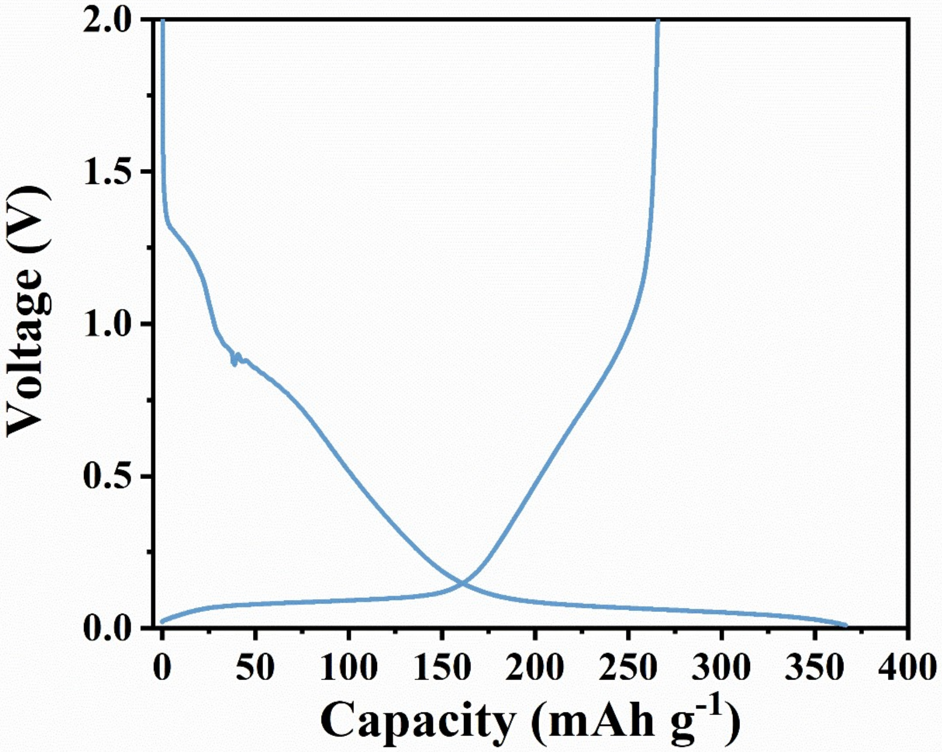

Fig. S37. The first charge/discharge curve of CHC.